Optimization of Impact Pile Driving Using Optical Fiber Bragg-Grating Measurements

Róisín M. Buckley[1]; Ross A. McAdam[2]; Byron W. Byrne[3]; James P. Doherty[4];
Richard J. Jardine[5]; Stavroula Kontoe[6]; and Mark F. Randolph[7]

Abstract: This paper reports the use of optical fiber Bragg-grating (FBG) sensors to monitor the stress waves generated below ground during pile driving, combined with measurements using conventional pile driving analyzer (PDA) sensors mounted at the pile head. Fourteen tubular steel piles with a diameter of 508 mm and embedded length-to-diameter ratios of 6:20 were impact driven at an established chalk test site in Kent, United Kingdom. The pile shafts were instrumented with multiple FBG strain gauges and pile head PDA sensors, which monitored the piles' responses under each hammer blow. A high-frequency (5 kHz) fiber optic interrogator allowed a previously unseen resolution of the stress wave propagation along the pile. Estimates of the base soil resistances to driving and distributions of shaft shear resistances were found through signal matching that compared the time series of pile head PDA measurements and FBG strains measured below the ground surface. Numerical solutions of the one-dimensional wave equation were optimized by taking account of the data from multiple FBG gauges, leading to significant advantages that have potential for widespread application in cases where high-resolution strain measurements are made. **DOI: 10.1061/(ASCE)GT.1943-5606.0002293.**

Introduction

Fiber Bragg-grating (FBG) sensors have been used previously to measure distributed strain during pile load testing on, e.g., large-diameter concrete piles (Schmidt-Hattenberger et al. 2003), bored piles (Lee et al. 2004), and jacked piles (Liu and Zhang 2012). The robust application of FBG sensors on impact-driven steel piles was demonstrated by Doherty et al. (2015) and the technology was used to measure soil–structure interaction during lateral load pile testing for the Pile Soil Analysis (PISA) project (Byrne et al. 2019; McAdam et al. 2019). The latter authors monitored the FBG sensors during pile driving at a rate of 1 kHz that, while relatively fast, could not provide high-resolution records of the traveling stress waves. Similar limitations on interpretation due to slow sampling rates were discussed by Baldwin et al. (2002) and Schilder et al. (2013).

FBGs are sections of an optical fiber that have been laser etched with a grating of a given period. The grating period is strain and temperature dependent; light with a wavelength corresponding to the grating period is reflected, while all other wavelengths pass the grating undisturbed. The change in wavelength of light reflected from the grating can be used to obtain the change in strain. The measured strain ε can be converted to force at each sensor for a section of known Young's modulus E and cross-sectional area A:

$$F = EA\varepsilon \qquad (1)$$

Measurements of force at multiple points along a pile under load can be used to obtain the base resistance and the distribution of shaft stress, in a similar manner to conventional strain gauges. Embedded strain gauges and accelerometers have been used to assess the shaft and base resistance during rapid load testing (e.g., Mullins et al. 2002) and dynamic testing (Tran et al. 2012). FBG sensor strings are placed and bonded into a pre-made groove in the pile, which represents an improvement over conventional electrical resistance strain gauges that often require substantial protection and cable channel sections, which can affect the subsequent load test behavior (Ciavaglia et al. 2017a). FBGs have high-strain capabilities combined with high-sampling-rate capabilities, which makes them suitable to capture the distributed strain response along the pile during pile driving.

Chalk is a generally structured very fine-grained porous weak carbonate rock, often encountered in northwest Europe during geotechnical investigations for ports, roads, railways, commercial/domestic buildings, and industrial plants/utilities, as well as offshore oil, gas, and wind-energy installations. While bored and continuous flight auger piles are selected for many applications, large open-ended driven piles are employed for most offshore and nearshore developments (Lord et al. 2002; Jardine et al. 2018). The encountered materials pose difficulties to engineers when designing these high-capacity, often large-diameter tubular steel piles. However, designers seeking to ensure satisfactory performance have

---

[1] Lecturer, Dept. of Engineering Science, Oxford Univ., Parks Rd., Oxford OX13PH, UK (corresponding author). ORCID: https://orcid.org/0000-0001-5152-7759. Email: roisin.buckley@eng.ox.ac.uk

[2] Professor, Dept. of Engineering Science, Oxford Univ., Parks Rd., Oxford OX13PH, UK. Email: ross.mcadam@eng.ox.ac.uk

[3] Professor, Dept. of Engineering Science, Oxford Univ., Parks Rd., Oxford OX13PH, UK. Email: byron.byrne@eng.ox.ac.uk

[4] Professor, Faculty of Engineering and Mathematical Science, Univ. of Western Australia, 35 Stirling Highway, Perth 6009, Australia. Email: james.doherty@uwa.edu.au

[5] Professor, Dept. of Civil and Environmental Engineering, Imperial College London, London SW7 2AZ, UK. Email: r.jardine@imperial.ac.uk

[6] Reader, Dept. of Civil and Environmental Engineering, Imperial College London, London SW7 2AZ, UK. Email: stavroula.kontoe@imperial.ac.uk

[7] Professor, Faculty of Engineering and Mathematical Science, Univ. of Western Australia, 35 Stirling Highway, Perth 6009, Australia. Email: mark.randolph@uwa.edu.au

Note. This manuscript was submitted on June 7, 2019; approved on February 24, 2020; published online on June 29, 2020. Discussion period open until November 29, 2020; separate discussions must be submitted for individual papers. This paper is part of the ***Journal of Geotechnical and Geoenvironmental Engineering***, © ASCE, ISSN 1090-0241.

J. Geotech. Geoenviron. Eng., 2020, 146(9): 04020082

Table 1. Summary of classification and index tests

Parameter	Margate chalk	Seaford chalk
Intact dry density, IDD (Mg/m^3)	1.42–1.64 (1.50)	1.38–1.51 (1.46)
Natural moisture content, w_c (%)	28–33 (30)	28–34 (30.5)
Degree of saturation, S_r (%)	90.3–100 (92.9)	96.7–100 (98.4)
Liquid limit, w_l (%)	24–25 (24.8)	30–32 (31)
Plasticity index, w_p (%)	5–7 (6)	7–8 (7.5)
Unconfined compressive strength, q_u (MPa)	2.1	2.0–2.8 (2.5)
Particle density, G_s (Mg/m^3)	2.71 (2.71)	2.71–2.73 (2.72)

Source: Data from Fugro (2012); SEtech (2007).

limited reference data regarding the axial and lateral capacities and stiffness response of such piles. Pile driving problems are also common. Ciavaglia et al. (2017a) report some of the only available lateral load tests in chalk. Recent research has aimed to advance the understanding of the axial behavior of displacement piles in chalk (Buckley et al. 2018a, b; Ciavaglia et al. 2017b) and has led to new preliminary design rules (Buckley 2018; Jardine et al. 2018). The axial-lateral pile analysis for chalk applying multiscale field and laboratory testing joint industry project (ALPACA JIP), described by Jardine et al. (2019), is underway to investigate a wide range of axial and lateral cyclic loading conditions through high-quality experiments on driven piles. A total of 14 of the piles were instrumented before driving with novel fiber optic strain gauges embedded along their shaft, as well as above-ground pile driving analyzer (PDA) strain gauges and accelerometers.

This paper reports the instrumentation, installation, and dynamic load testing of the 508-mm-diameter open-ended tubular steel ALPACA piles installed into a chalk profile, which had both FBG and pile head-mounted PDA measurements during driving. The measurement frequencies in both sets of instruments were such that the stress waves generated by the hammer impacts could be tracked down the pile by the FBG strains during driving. These steps allowed novel comparisons to be made between the distributed forces along the pile, as measured by the FBG instruments, and those assessed from the PDA data through one-dimensional stress wave theory. An optimization process was developed to improve the match between measured and calculated distributed forces.

Site Description

The ALPACA project involved driving open-ended tubular steel piles at a chalk quarry test site located close to the village of St. Nicholas at Wade, Kent, United Kingdom (UK Grid TR 25419 66879). The site has been used previously to advance understanding of displacement piles in chalk (Buckley et al. 2018a, b; Ciavaglia et al. 2017a, b). A new geotechnical site investigation, which included piezocone penetration tests (CPTs) with pore water pressure measurement to 14.9 m, seismic CPTs to 15.2 m and Geobore-S boreholes to 15.5 m was carried out for ALPACA, in close proximity to the test piles.

The Margate white chalk subgroup is encountered from the ground surface, while the Seaford chalk formation is encountered from ≈1.6 m below ground level (mbgl). Table 1 gives a summary of classification and index test results within the depth of interest. The chalk classifies as low-medium density [intact dry difference $(\mathrm{IDD}) = 1.38–1.64\ \mathrm{Mg/m^3}$] structured grade B3-A2 material with small-to-medium-sized flints within the current classification system (Bowden et al. 2002). Unconfined compressive strength (UCS) tests show q_u values of 2.0–2.8 MPa, within the range expected for low-medium density material given by Matthews and Clayton (1993). Although the water table is located at ≈6 mbgl, the degree of saturation above this is between 90% and 100%. Two flushable piezometers installed in boreholes confirmed the water table depth and the presence of negative pore water pressures above the water table. Independent temperature measurements at the same depths as the piezometers indicated ground temperatures of between 11°C and 13°C.

Fig. 1 shows a typical CPT profile from the site within the depth of interest of the test piles. The corrected cone resistance q_t varies typically from 10 to 20 MPa above 8 m depth, increasing to between 10 and 30 MPa with depth. Sleeve friction f_s is typically

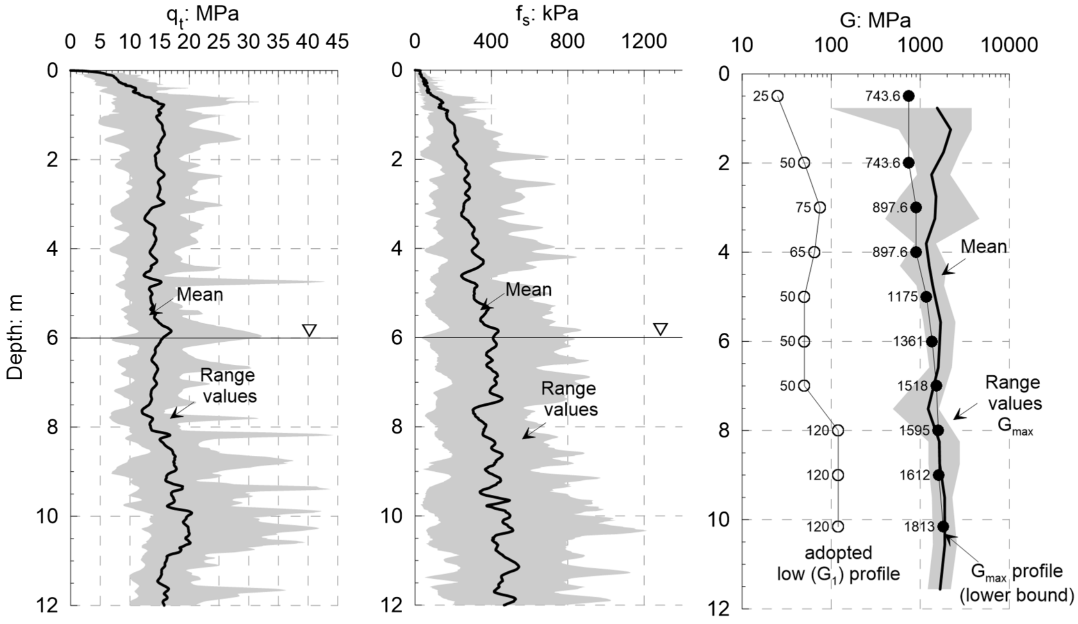

(a) (b) (c)

Fig. 1. Site profiles of (a) CPT cone resistance q_t; (b) CPT sleeve friction f_s; and (c) shear modulus measured in seismic CPTs.

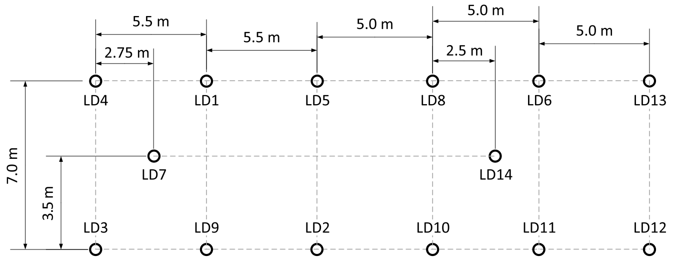

Fig. 2. Plan of pile installation layout.

between 200 and 500 kPa and increases slightly with depth. Excess pore water pressures (not shown) are remarkably high, ranging from 2 to 6 MPa at the shoulder (u_2) position; still higher values up to 12 MPa are possible at the tip (u_1) position (Buckley et al. 2018b). A total of 28 dissipation tests were conducted at various depths that showed time for 50% pore water pressure dissipation t_{50} of between 2 and 4 s and equivalent coefficients of horizontal consolidation c_h of $1.5–3.0 \times 10^{-3}$ m^2/s, assuming high-rigidity indices for the chalk and following Teh and Houlsby (1991). Fig. 1(c) shows the range of shear modulus ($G_{\max}$ or G_{vh}) obtained from seismic CPT measurements. The shear modulus typically ranges from 700 to 2,400 MPa, with significant scatter observed in measurements taken in the top 3 m.

Test Pile and Instrument Specifications

Pile Details

A total of 13 instrumented 508-mm-diameter open-ended tubular piles made from high-yield-strength steel (API 5L Grade X80) with a wall thickness t_{wall} of approximately 20.6 mm were driven in November 2017. The high-yield steel was selected to allow geotechnical failure to be achieved before the steel walls yielded in the lateral load tests. Prior to installation, the roughness of the outer pile surface was measured using a Mitutoyo Surftest SJ-210 device (Mitutoya, Takatsu-ku, Japan). A total of 59 measurements on 13 piles showed a mean average center-line roughness R_a of 15.4 μm with a standard deviation of 3.9 μm.

Fig. 2 shows the pile layout plan. A total of 11 of the piles penetrated to 10.16 m depth, with approximately 40% of their shaft length below the water table. The remaining two piles reached 3.05 m depth and were fully installed above the water table. The piles were driven using a Junttan SHK 100-3 4T (Junttan Oy, Kuopio, Finland) hydraulic impact hammer. The long piles ($L/D = 20$) were driven at ≈ 2 blows/s and penetration rates of up to 23 mm/s. The short piles ($L/D = 6$) were installed in less than 2 min with approximately 100 blows. Fig. 3 shows the blow count profiles. Considering the piles as open-ended with equivalent radii R^* gives normalized pile installation velocities of 0.32–0.36, and installation was probably partially drained according to the interpretation given by Buckley et al. (2018a). The piles were fully coring, with the final internal chalk columns extending 0.5 and 1.1 m above ground level for the short and long piles, respectively. Pauses in pile driving in chalk can lead to increases in shaft resistance [e.g., Dührkop et al. (2017)]. A driving dolly was used to ensure that the rising chalk column did not come into contact with the hammer and cause driving interruptions. An additional long pile (LD14) was installed in the same way in May 2018.

Instrumentation

Fig. 4 shows the geometry and layout of instrumentation on the long and short LD piles. Strain gauges and accelerometers were attached near the pile heads to give information on the force and velocity at the pile top for each hammer blow (Fig. 5). The PDA gauges were installed prior to driving and the dynamic driving data was acquired continuously during installation using proprietary software. The PDA measurements, taken 1.0 m below the pile head, were sampled at a frequency of 40 kHz to allow a detailed time history to be obtained for each blow.

The FBG instrumentation was installed by the specialist subcontractor Marmota Engineering prior to transport to site. A horizontal boring machine was used to machine 5-mm-square grooves into the piles, into which the FBG sensors were fixed. The quantity of steel

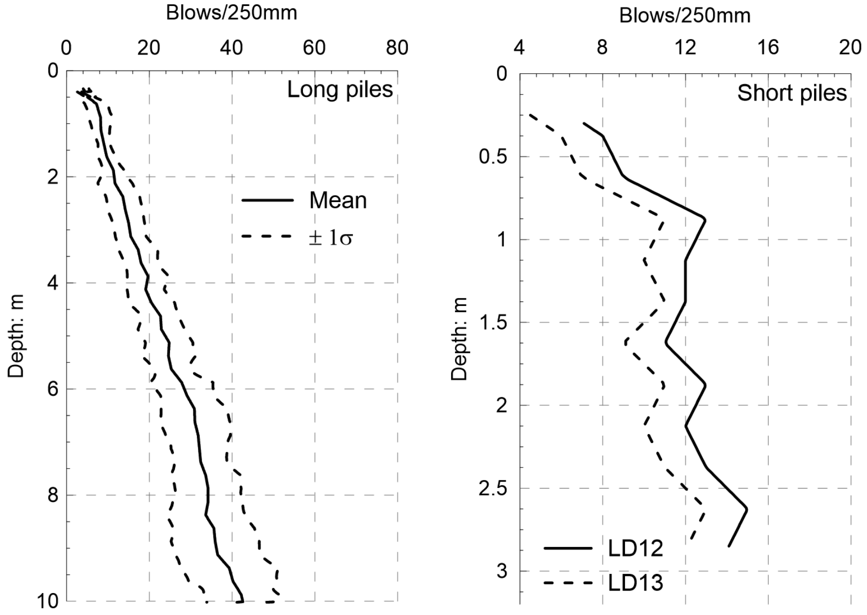

Fig. 3. Penetration records measured during pile driving.

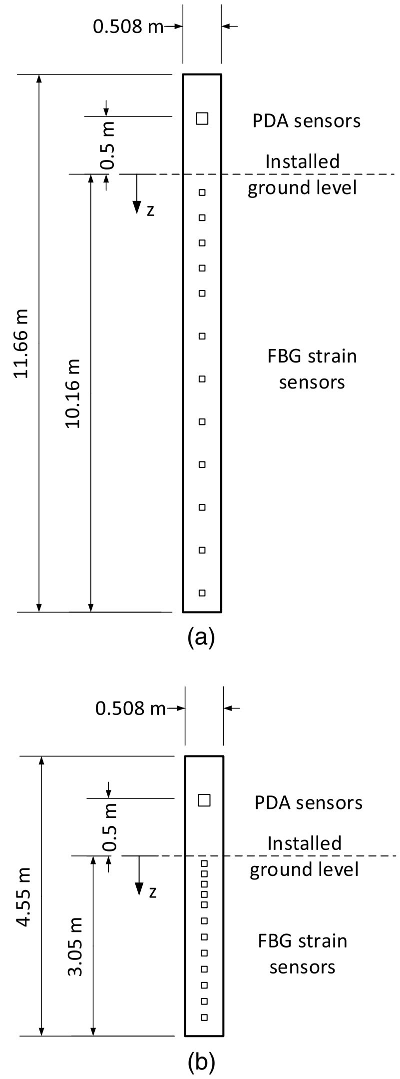

Fig. 4. Pile geometry and sensors' layout.

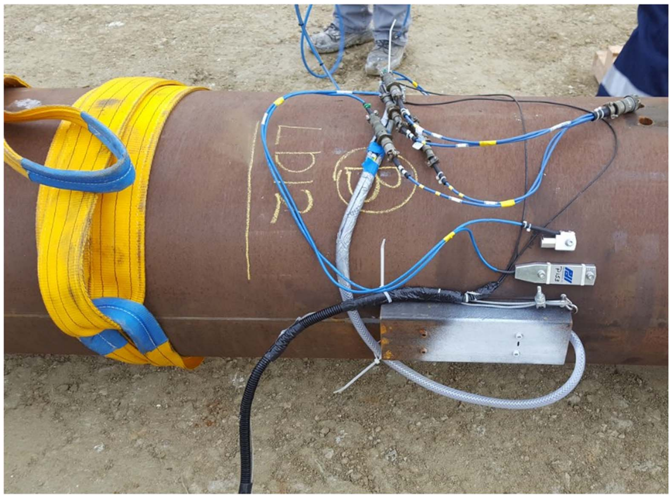

Fig. 5. Pile driving analyzer instrumentation and fiber optic readout on LD12 prior to driving.

Table 2. FBG sensor pile locations

Gauge horizon number	Position below installed ground level, z (m)	
	Long LD pile	Short LD pile
1	0.5	0.15
2	1.0	0.30
3	1.5	0.45
4	2.0	0.60
5	2.5	0.75
6	3.5	1.05
7	4.5	1.35
8	5.5	1.65
9	6.5	1.95
10	7.5	2.25
11	8.5	2.55
12	9.5[a]	2.85

[a] LD14 included a temperature sensitive fiber optic gauge mounted on to the pile face at 9.4 m.

cross section removed as a result of the machining is negligible (<0.1%) and has little effect on the structural properties adopted for the driving analysis or subsequent load testing. Each groove encapsulated 12 strain gauges in a single string that was pretensioned to approximately 1,000 $\mu\varepsilon$ and potted into place using an epoxy resin. An additional layer of hot-gun glue was then applied as a sacrificial layer of protection during driving. Only the sensor lead-out cable required any external steel protection (Fig. 5), and the pile profile remained cylindrical without any protruding protection channeling. LD1–LD13 were each instrumented with diametrically opposed strings of FBG sensors spaced as shown in Fig. 4 and Table 2. The selection of the relatively large pile wall thickness and the instrumentation levels was driven by the requirements for the subsequent lateral load testing, where the variation of the bending moment and resulting strain is greatest toward the ground level, and a greater density of sensors is required. The number of sensors was selected to allow sufficient change in frequency, given the expected strain levels during subsequent load testing and the constraint of a limited bandwidth from the fiber optic interrogators.

The total strains measured by the FBGs include the actual mechanical strain as well as strains induced due to both the thermo-optic effect and the thermal expansion of the composite (steel-adhesive-fiber) material. FBG temperature sensing during driving of previous projects indicated difficulties in achieving full strain insensitivity, and so it was decided to omit temperature measurements from all but one test pile at the site. LD14 was instrumented with four strings spaced circumferentially around the pile, each including an FBG temperature sensor close to the bottom strain sensor. A post-test program temperature calibration on LD13, where the pile was subjected to uniform temperature changes under zero load, indicated an average change of 22 $\mu\varepsilon/°\mathrm{C}$ (≈ 150 kN/°C) during a temperature increase of 35°C.

The reflected wavelengths were sampled and converted to engineering strains using a Micron Optics si155 interrogator (Micron Optics, Atlanta). The interrogator has four channels, each of which can monitor all the strain gauge levels down a given string; so, the dynamic monitoring required two channels for the piles with two fiber optic strings and four for pile LD14 with four strings. Strain measurements taken when the piles were laying on the ground before being pitched have been used to set the initial zero-strain values presented in this paper. During driving, the piles were logged continuously at a sampling frequency of 5 kHz (the highest

J. Geotech. Geoenviron. Eng., 2020, 146(9): 04020082

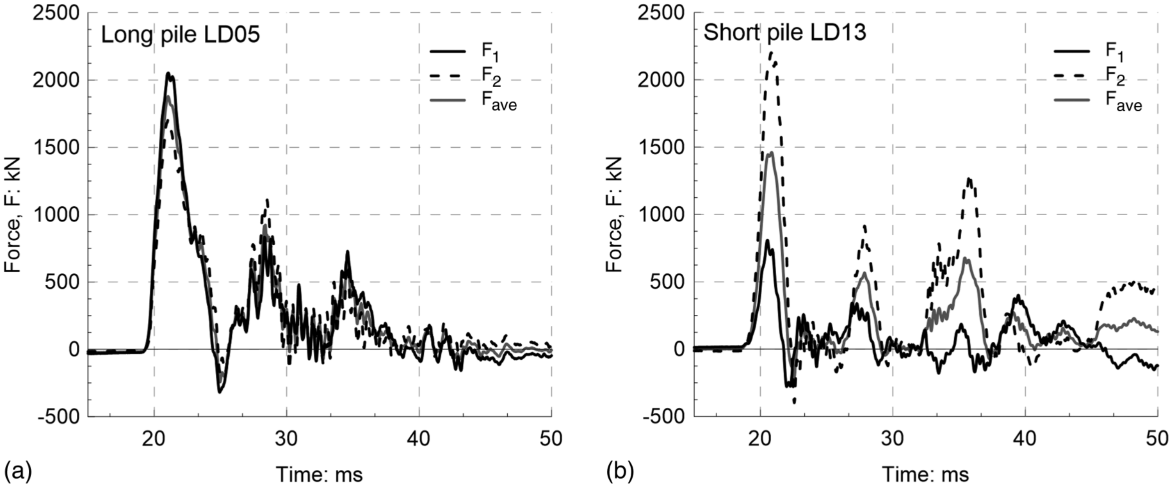

Fig. 6. PDA force measurements for a blow at the end of driving: (a) long pile LD05; and (b) short pile LD13 (F_{ave} = average of force, F_1 = force on side 1, and F_2 = force on side 2).

sampling rate offered by an interrogator at the time of pile driving), which was reduced to 100 Hz after the end of driving (EOD). Note that the 5 kHz frequency is that for *each* strain gauge level down a given string. A fast Fourier transform performed on the PDA and FBG data indicated that while the sampling rates result in some force amplitude being missed at the higher frequencies (i.e., above 2.5–2 kHz), these amplitudes are orders of magnitude smaller than the main signal. All FBGs were fully operational at the end of the driving process. Note that the rise time of 2 ms noted later would suggest a dominant frequency around 125 Hz.

Measurements During Pile Driving

Dynamic Monitoring

In stress wave analysis, the accelerations measured during and after each hammer blow are integrated to give velocity v and displacement of the pile with time. The strains ε measured by the PDA gauges are used to obtain the force via Eq. (1). Above ground level, the resulting traces of F and Zv [where Z is the pile impedance ($= EA/c$) and c is the wave propagation speed] are equal until waves reflected from soil tractions or changes in the pile cross section arrive back at the measurement location. Numerical methods, such as the method of characteristics (Middendorp 1987), are used to solve the one-dimensional wave propagation equation. The measured F or Zv signals can be used as the input boundary condition, eliminating the need for hammer modeling. Alternatively, the two signals may be combined to obtain the downward-traveling component of the stress wave, fitting the numerical solution to the upward-traveling component.

The downward- and upward-traveling wave components are calculated from

$$F_{up} = \left(\frac{F - Zv}{2}\right) \tag{2}$$

$$F_d = \left(\frac{F + Zv}{2}\right) \tag{3}$$

The reflected traces from below ground level are affected by the static and dynamic soil or rock resistances, and simplified rheological models are used to simulate their effects by applying combinations of springs, dashpots, and plastic sliders.

Fig. 6 shows examples of the force measurements made with the PDA gauges mounted on short and long examples of the ALPACA piles during hammer blows applied toward the EOD. The time for the first increase in force t_0 was $\approx$19.2 ms, while the time for maximum F, t_m was $\approx$21.2 ms, indicating a rise time of 2 ms. The force and acceleration data were measured on both sides of the pile; the averages of the F and Zv measurements from the two sets of gauges were adopted for input into the analysis. A schematic of the downward-traveling wave and measured reflections at the PDA gauges at the pile top is shown in Fig. 7, along with the upward-traveling force F_{up} calculated from the EOD hammer blow shown in Fig. 6(a). Taking a steel mass density ρ of 7.8 Mg/m^3 and Young's modulus E of 210 GPa leads to a pile impedance Z of 1,277 kNs/m.

Fiber Optic Measurements

The fiber optic gauge measurements for sides A and B and their average is shown in Fig. 8 for the top (Level 1) gauges under the hammer blows plotted in Fig. 6. The FBG data has a different reference time point compared to the PDA measurements; due to incompatibility of time synchronization between the PDA and fiber optic interrogators during acquisition, the measured signals were synchronized during postprocessing. The data shown in Fig. 8 corresponds to PDA time; the offset accounts for the peak-to-peak travel time from the PDA gauge to the relevant FBG. A similar magnitude of force is apparent, with the FBGs located at 1.0 and 0.65 m below the PDA gauges on the long and short piles, respectively. Fig. 9 shows the time history during all the 832 driving blows required to install pile LD05, in terms of the force calculated from the average strain at the top gauge level from the two fiber optic strings. The initial seating blows were followed by a short pause in driving, during which the pile's verticality was checked and adjusted. In contrast to the PDA measurements, where F and Zv returned close to zero at the end of each blow, the FBG measurements typically recorded a non-zero measurement at the end of the blow. This zero-drift residual strain was observed after most blows, at all gauge levels, in both tension and compression. The magnitude of the residual strain tended to increase with continued driving. Fig. 10 shows a typical variation of the zero-drift in

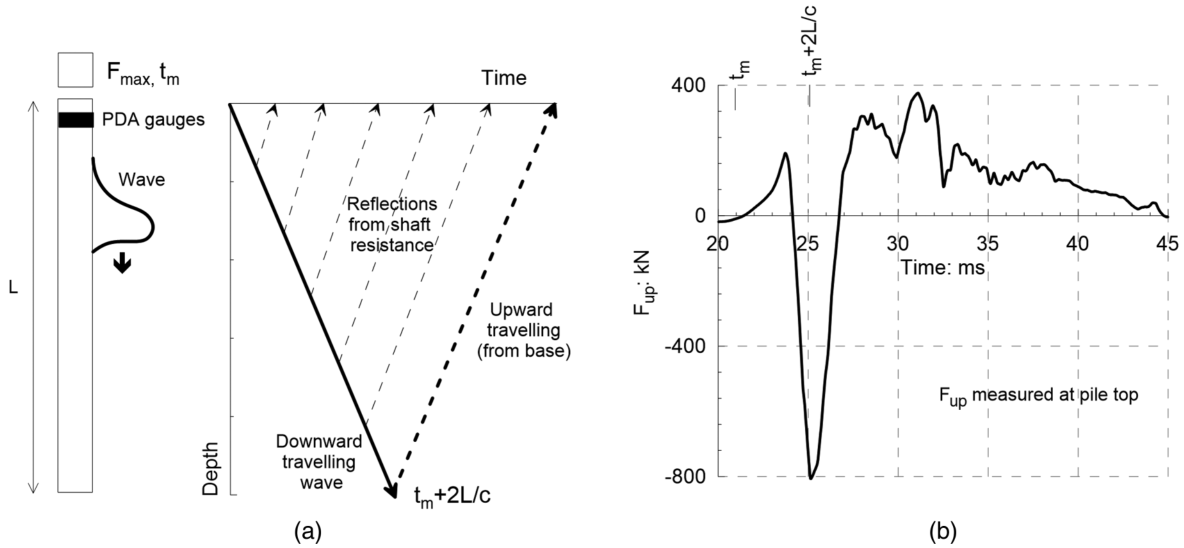

Fig. 7. (a) Schematic of downward-traveling wave and measured reflections from PDA measurements; and (b) upward-traveling wave calculated using data from Fig. 6(a).

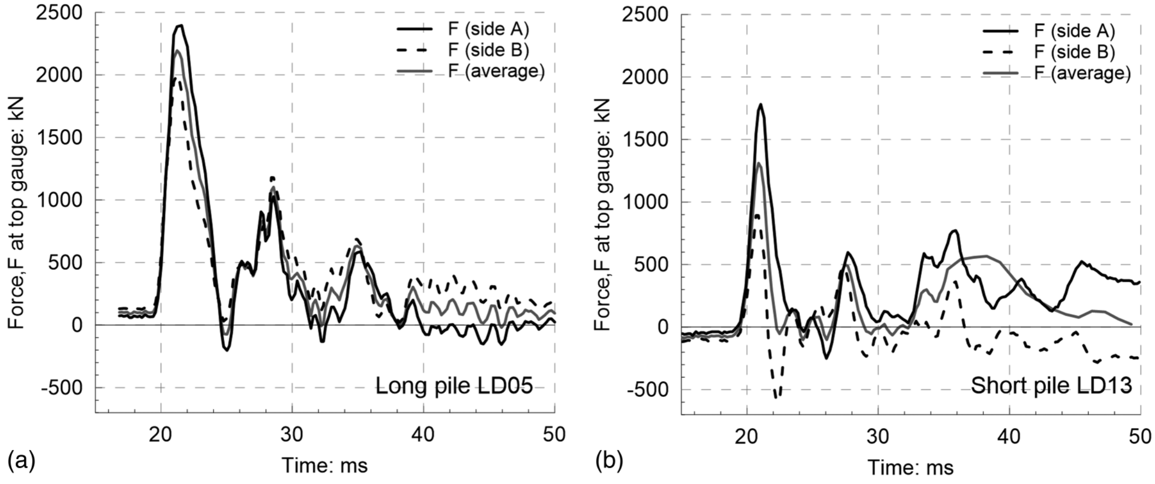

Fig. 8. Force measurements at the top fiber optic strain gauge for a blow at the end of driving: (a) long pile LD05; and (b) short pile LD13.

strain and equivalent force at each gauge level for three stages during driving and at EOD, illustrating for this case a gradually increasing residual compressive force with depth.

Residual or locked-in compressive axial forces are expected after a driving blow, as the pile rebounds and negative shaft resistance is mobilized to maintain static equilibrium. The magnitude and distribution of residual loads are influenced by the pile's total capacity, the ratio of shaft and base capacity, and the pile material and geometry and are typically concentrated in the lower half of the pile to balance residual tip forces (Maiorano et al. 1996). Residual loads can be significant when the base capacity is similar to the shaft capacity, as in sands (Briaud and Tucker 1984). Residual loads are thought to be low during the driving of large-diameter fully coring tubular piles (Byrne et al. 2018) for which large locked-in tensile loads are not expected. The zero-drift observed may be a result of (1) locked-in stresses in the steel or in the steel groove which are shaken down during driving, and/or (2) changes in strain due to changes in temperature, shown by calibration to be significant, as the pile transmits heat to the surrounding chalk. A single pile LD14 was equipped with a fiber optic temperature sensor 0.1 m above the bottom gauge which showed a temperature drop of 9.2°C during driving on a sunny day that had prewarmed the pile's lightly rusted surface to a marked degree. It was noted that due to the large pile wall thickness, small deviations in strain result in significant apparent locked-in pile forces; each 1 $\mu\varepsilon$ measured equates to 6.6 kN of force. Fig. 10(c) shows that the accumulation of residual force is accompanied by an accumulation of residual bending moment along the pile, about an axis perpendicular to that of the strain gauges.

Due to significant uncertainty in disaggregating the contributions to the accumulated residual pile forces of the temperature, steel stresses, and chalk shaft shear stresses, it was felt appropriate to re-zero the strain at the beginning of each blow to aid initial interpretation, as illustrated in Fig. 11, which shows the strain time history for the EOD blows on piles LD05 and LD13. This treats any locked-in stresses due to soil-pile interaction as being small, relative to the stresses induced by the impact shockwave, and the temperature variations over the short period of observation time for a hammer blow. No attempt was made to correct the strain measurements made on LD14 for temperature sensitivity.

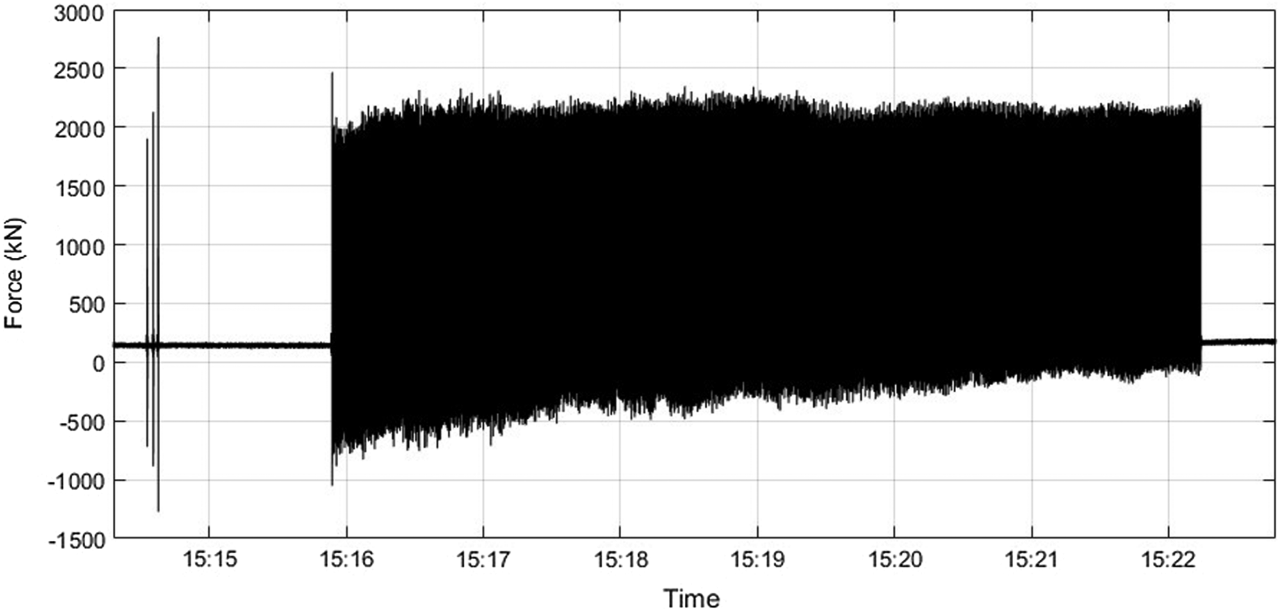

Fig. 9. Force time history based on averaged top FBG measurements during driving of pile LD05.

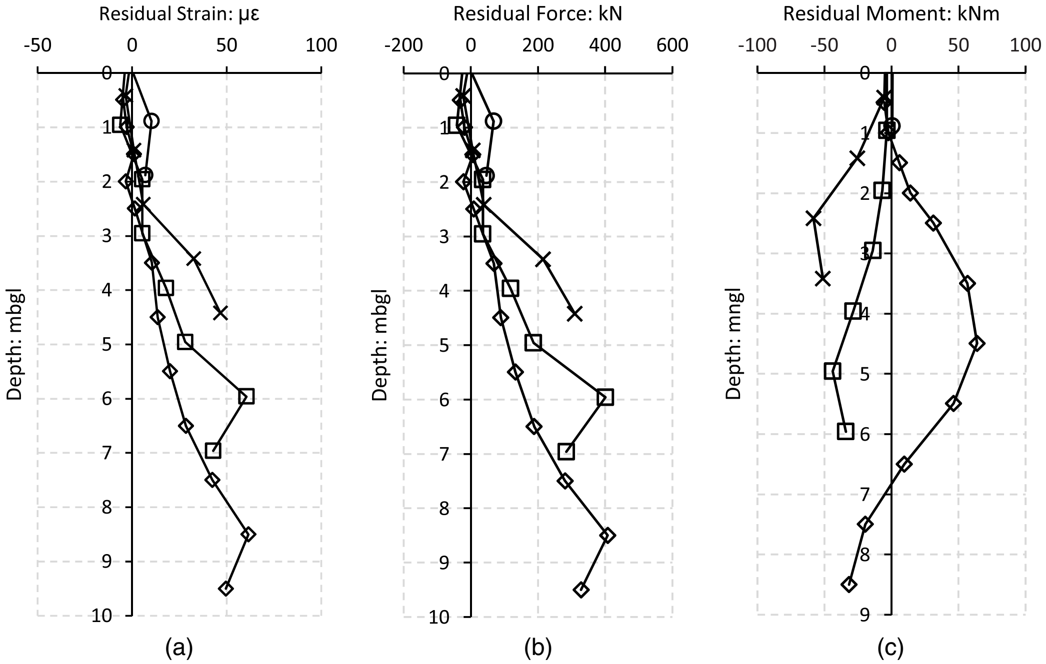

Fig. 10. Variation of apparent depthwise average residual strain, force, and moment during the driving of pile LD05.

Analysis of Dynamic Measurements

Conventional stress wave matching is carried out through numerical analyzes that apply (in this case) the known downward-traveling waveforms to the pile top and output predictions for the responding upward-traveling waves by applying specified pile shaft and base resistance models. The parameters defining the resistance models are varied iteratively until a good match is obtained between the artificially generated stress wave (in this case the upward-traveling wave) and those measured by the pile head sensors. This leads to base and shaft resistance assessments for each blow analyzed. At each node, the axial force in the pile at time $t + \Delta t$ is calculated from the arriving upward- and downward-traveling velocities v_d and v_{up}, modified by the total shaft or base resistances acting at the node in question.

While the PDA system was used to acquire the data, the research-oriented software program IMPACT (Randolph 2008) was used to analyze the dynamic measurements. IMPACT employs shaft and base resistance models based on elasto-dynamic theory (Deeks and Randolph 1995; Simons and Randolph 1985) as summarized in Table 3. The input parameters into the resistance models include the shaft stress distribution and base resistance as well as

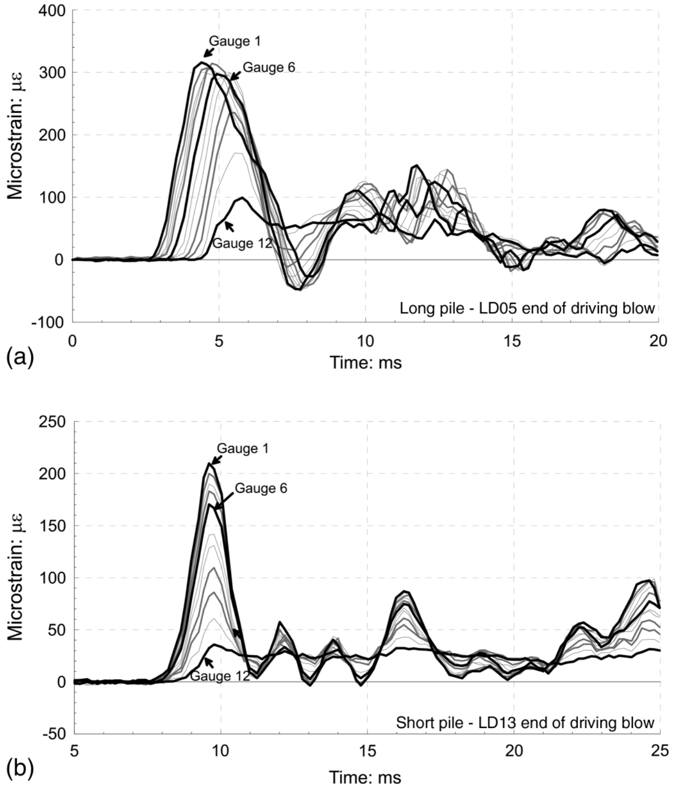

Fig. 11. Strain time history from depthwise averaged FBG measurements for the end of driving blow: (a) long pile LD05; and (b) short pile LD13.

Table 3. Summary of equations and adopted models in IMPACT

Shaft model (Randolph and Simons 1986; Simons and Randolph 1985)	Shaft resistance	$\tau = k_s w + c_s v \le \tau_{stat}$
	Spring	$k_s = \dfrac{G}{\pi D}$
	Radiation dashpot	$c_s = \dfrac{G}{V_s} = \sqrt{G\rho_s}$
	Viscous effects	$\tau_{inter} = \tau_{stat}\left[1 + \alpha\left(\dfrac{\Delta v}{v_0}\right)^{\beta}\right]$
Base model (Deeks and Randolph 1995)	Base resistance	$Q_b = K_b w + C_b v \le Q_{b,stat}$
	Spring	$K_b = \dfrac{4GR}{(1-\nu)}$
	Radiation dashpot	$C_b = \dfrac{4R^2}{(1-\nu)} 0.8\sqrt{G\rho_s}$
	Subsidiary mass	$m_0 = 0.16\dfrac{4R^3\rho_s}{(1-\nu)}$

the chalk density ρ_s, shear modulus G, and shaft viscosity parameters α and β (Randolph 2008). Note that the latter two parameters define viscous enhancement of the limiting shaft friction based on the *relative* pile-soil velocity, rather than the absolute pile velocity.

Input Parameters

The chalk density and shear modulus G were determined for input into IMPACT from the ALPACA site investigation. The values of G were secant values G_1 degraded from the very high small strain $G_{\max}$ values recorded by in situ seismic CPTs to account indirectly for soil nonlinearity, following Alves et al. (2009) and noting that the chalk is markedly brittle and produces a very soft annulus of putty around the shaft during driving (Buckley et al. 2018a). As such, the G_1 values were reduced to less than 10% of the lower range of the $G_{\max}$ profiles recorded on site, as shown in Fig. 1(c). The shaft viscosity parameter β was taken as 0.2, consistent with the recommendations of Randolph (2008). The adopted value of α of 1.1 was determined using the correlation given by Loukidis et al. (2008), taking s_u from remolded samples to reflect the soft behavior expected in the annulus of chalk putty close to the shaft. IMPACT includes explicit modeling of internal shaft resistance (Randolph 2008). Earlier signal-matching studies by Buckley (2018) have shown that fully coring piles develop little shaft resistance on their internal areas during driving in chalk. Internal shaft resistance was assumed to be negligibly small and concentrated close to the tip of the pile, and thus, indistinguishable from the overall lumped tip resistance. The residual base stresses were also set to zero for the dynamic analysis presented in the following text.

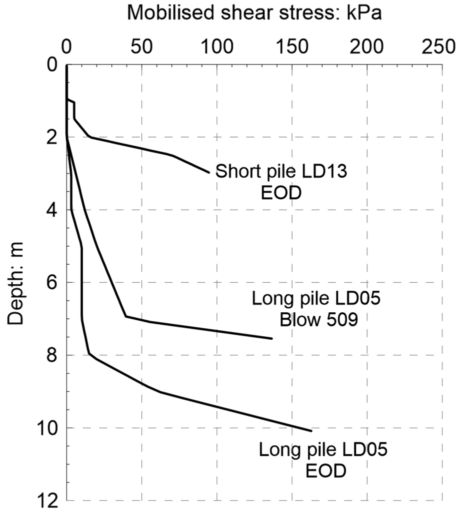

Fig. 12. Depthwise shaft friction profile obtained by manual signal matching.

Signal Matching of Individual Blows

Signal matching was carried out by comparing the time series of the measured F_{up} with the numerical upwave created using the downwave force signal from the hammer as input. The measured pile head displacement was also compared to the computed displacement. The reflections due to shaft and base resistance and the upward-traveling are shown previously in Fig. 7. Fig. 12 shows examples of the local shaft resistance with depth interpreted from the dynamic measurements made on the exemplar long pile LD05 at the end of, and during, driving and on the exemplar short pile LD13 at EOD. A trial signal match is illustrated in Fig. 13 for LD05 in terms of the measured (through PDA) trace for F versus the predicted top Zv signal and the measured-versus-calculated pile head displacement. This match predicts that most of the shaft resistance was mobilized over the bottom 20% of the pile shaft, with <15 kPa mobilized over the upper 80% of the pile. A sharp tendency for the local shaft shear stress to attenuate with increased pile penetration (known as friction fatigue or the h/R effect) is evident from Fig. 12, following trends also observed in chalk by Buckley et al. (2020) at other sites.

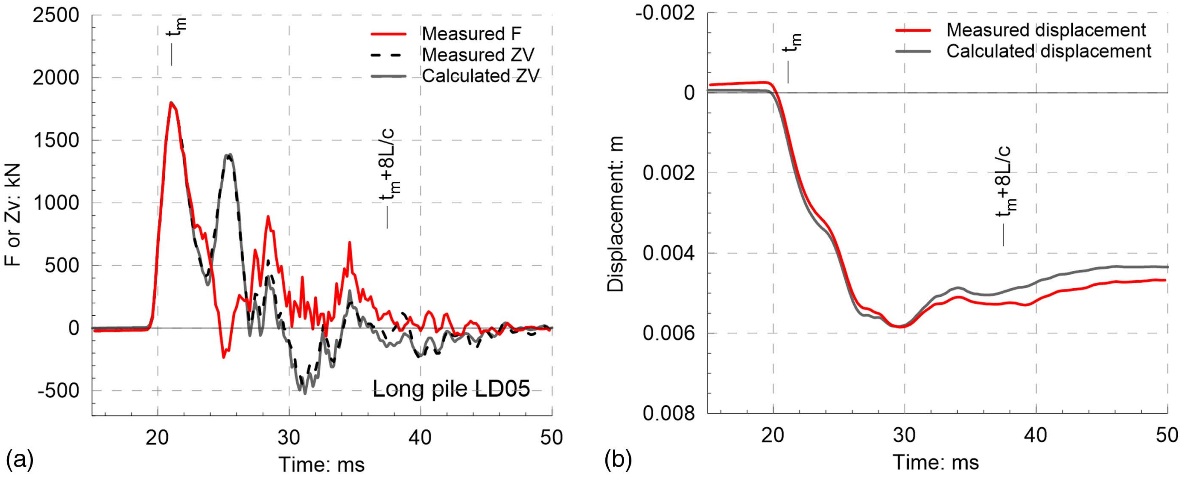

Fig. 13. Example of measured (through PDA) and calculated (IMPACT): (a) F and Zv at the pile head; and (b) displacement at the pile head.

Base resistance was interpreted as applying over only the annular tip areas of the fully coring open-ended piles, and the resulting bearing pressure q_{ba} was taken as a proportion of the local cone resistance q_t. The variation between measured pile displacements for the blows considered in this study was relatively small, with average values of $\approx 14.4 \pm 5.3$ mm, i.e., $2.8\% \pm 1.0\%$D, but $75\% \pm 26\%$ of the pile wall thickness; the tip resistance was taken as a constant factor of 0.6 relative to the cone resistance.

The signal-matching process does not lead to unique solutions. Multiple parameter sets can be proposed that provide similar degrees of fit to the measured signals, leading to interpretations that are inevitably subjective (Buckley et al. 2017; Fellenius 1988). The novel FBG measurements reported here provide additional information to which the numerical solutions must conform, which enables the analysis to be refined. The need to match the forces calculated by IMPACT at 12 additional nodes further constrains the possible solutions to a very considerable degree, as illustrated in Fig. 14. Fig. 15 shows the forces measured at the top, middle, and bottom gauges at the end of driving, along with the calculated force from IMPACT at the relevant depth for piles LD05 and LD13. The corresponding match to the stress wave data measured at the pile top was shown previously in Fig. 13. In this case, good coincidence is seen between the measured and calculated force time histories along the main pile length, which gives confidence in the proposed trial signal-matching parameters. However, the forces recorded by the FBG bottom gauge are less reliably predicted, particularly over the latter portions of the record.

Calibration of Dynamic Analysis Using FBG Measurements

The novel FBG measurements undertaken during pile driving open up further avenues for optimizing the dynamic analyzes to enable more robust predictions of the distributions of shaft shear resistances during driving. An automated optimization procedure was developed to find the values of shear resistance that led to the lowest magnitude of difference between (1) the force measured at each gauge and the force calculated from IMPACT at the same level and (2) the upward force measured at the pile head and that calculated from IMPACT. During the subsequent optimization, the error in the single upward-force measurement at the pile head was weighted equally to the sum of the errors between the strain gauge inferred pile forces and the pile forces calculated from IMPACT.

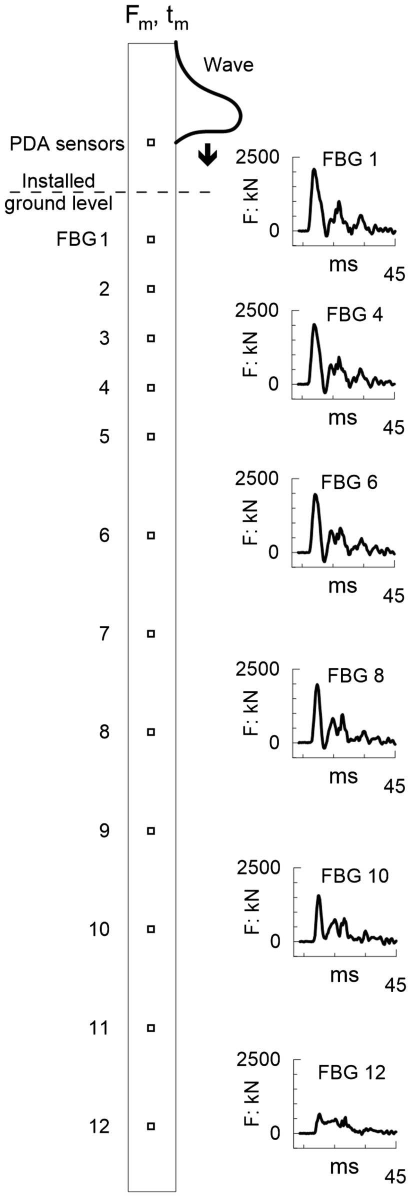

Fig. 14. Schematic of measured force at each FBG horizon.

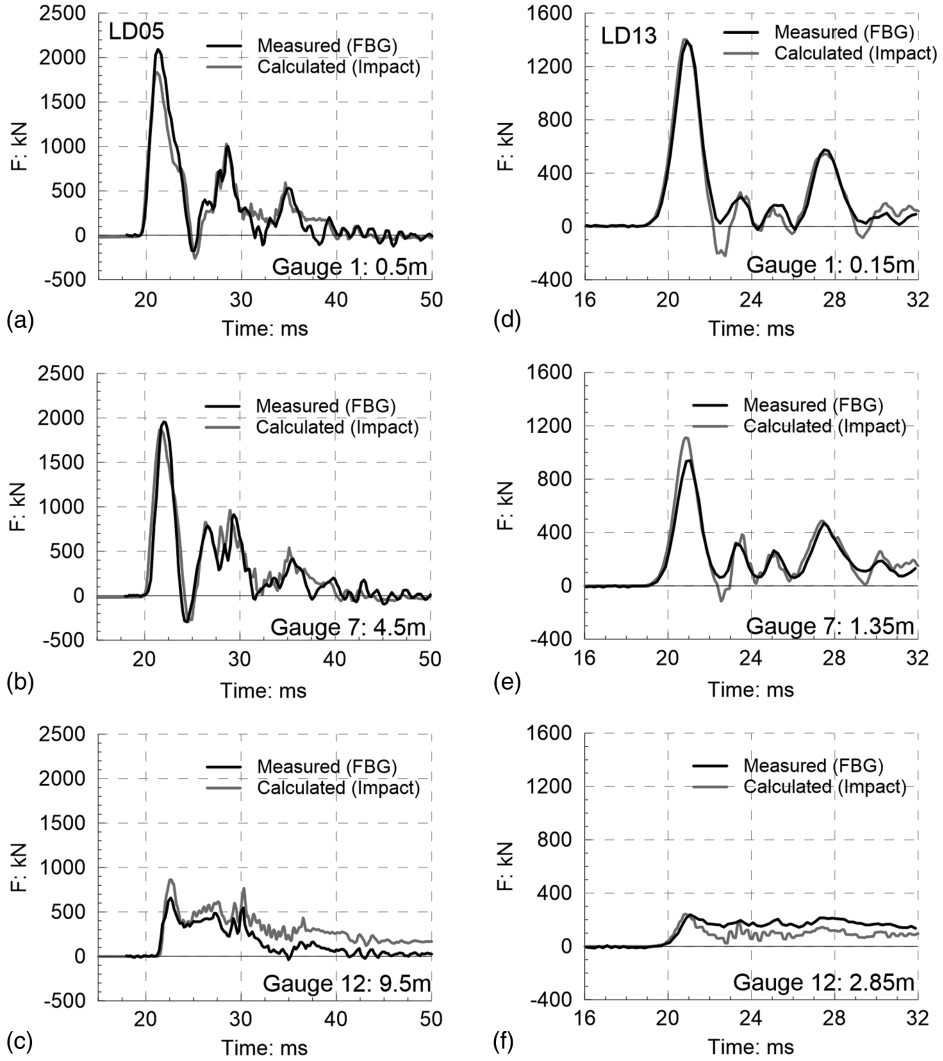

Fig. 15. Comparison of measured and predicted stress waves at end of driving using manual signal matching: (a) Gauge 1 LD05 EOD; (b) Gauge 7 LD05 EOD; (c) Gauge 12 LD05 EOD; (d) Gauge 1 LD13 EOD; (e) Gauge 7 LD13 EOD; and (f) Gauge 12 LD13 EOD.

The accuracy of an overall individual match can be quantified by comparing normalized values of the measured and calculated error. The overall normalized error is expressed as

$$\zeta(\%) = 0.5 \times \frac{1}{n}\sum_{i=1}^{n}\frac{\zeta_f(i)}{F_{\max}(i)} + 0.5 \times \left(\frac{\zeta_{f,up}}{F_{up,max}}\right) \tag{4}$$

where n = number of strain gauge horizons; over a given blow, ζ_f = average root mean square error between the measured and calculated force at each strain gauge horizon; F_{max} = maximum force measured at each strain gauge; $\zeta_{f,up}$ = average root mean square error between the measured and calculated upward force at the pile head; and $F_{up,max}$ = maximum measured upward force at the pile head. The normalized error can be assessed in various ways. In this analysis, it was found that giving equal weighting to the sum of the errors at the individual gauges and the error in the upward force at the pile head led to good matches between force at the gauges, as well as the measured and calculated quantities at the pile head. Omitting the pile head data from the matching process reduced the signal match quality. Equally, increasing the weighting of the error in the upward force at the pile head led to an increase in the overall normalized error.

The optimization process is illustrated by considering examples in which the distribution of shaft resistance is varied, while the viscosity parameters α and β are fixed at 1.1 and 0.2, respectively, and the base resistance at $0.6q_t$. The shear modulus applied in the spring and dashpot system dominates the behavior at each node prior to pile-chalk slip. Following slip, the pile resists at its limiting friction, augmented by viscous effects (Randolph and Simons 1986). The effect of varying the fixed proportion of the maximum shear modulus adopted was checked by optimizing an extreme $G = G_{max}$ profile and the secant G_1 profile (both shown in Fig. 1) to account indirectly for soil nonlinearity, which led to the successful manual matches at the pile head illustrated previously in Fig. 13. In addition to the EOD blow (832), shown previously for LD05, three additional middriving blows were considered in the optimization process (Blow 83 at 2.5 m penetration, Blow 246 at 5.1 m penetration, and Blow 509 at 7.6 m penetration). The initial shear resistance profiles for the middriving blow had similar shapes to the EOD initial estimate.

The following cases were considered for optimization of each blow described previously:

1. Where only the PDA data was used as input, i.e., optimizing an objective function featuring the second term in Eq. (4),

Table 4. Comparison of normalized error obtained by manual signal matching and optimization using PDA data only

		PDA input only ζ (%)	PDA input only ζ (%)		PDA and FBG input ζ (%)	
Stage (blow)	Depth (m)	No optimization	1a $G = G_{\max}$[a]	1b $G = G_1$[b]	2a $G = G_{\max}$[a]	2b $G = G_1$[b]
¼ complete (83)	2.5	8.4	5.0	4.9	5.0	4.9
½ complete (246)	5.1	7.3	6.3	4.4	6.2	4.3
¾ complete (509)	7.6	6.0	5.1	4.9	5.0	4.4
EOD (832)	10.2	6.0	5.2	5.0	5.1	4.1

[a] Profile of maximum shear modulus shown in Fig. 1.
[b] Profile of secant shear modulus shown in Fig. 1.

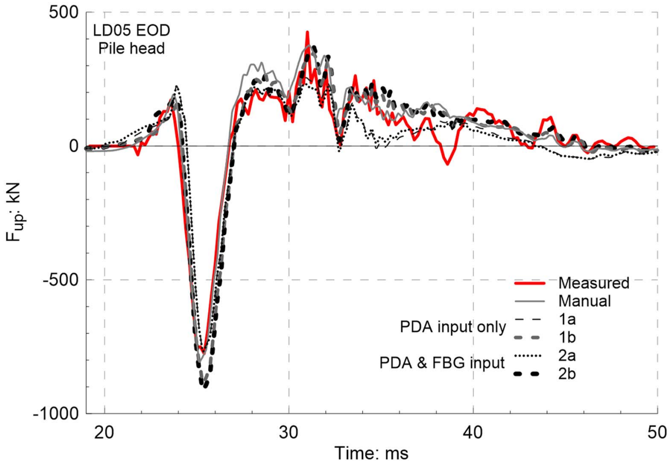

Fig. 16. Measured upward wave at LD05 EOD compared with calculated upward wave from IMPACT for no optimization and four optimization cases (Table 4).

attempting to improve the manual signal matches described earlier for both the high (1a) and low (1b) shear modulus cases.

2. Where both the PDA and FBG data were used as input, optimizing using both terms in (4) for both the high (2a) and low (2b) shear modulus cases.

Only the shear resistance τ values were allowed to vary nonuniformly with depth between the bounds of $0 < \tau < 300$ kPa using the Matlab *patternsearch* function, in which the value of (4) was minimized. The initial estimate was based on the manual analysis results shown in Fig. 12 and set for shaft shear resistance of 10 kPa at each node (at 0.5 m intervals) along the pile length, except for the toe node, where 200 kPa was applied.

Table 4 summarizes the normalized errors calculated using (4), obtained using both manual signal matching and the optimization cases detailed previously. The results indicate that in all cases, the overall normalized error is reduced significantly by the optimization process. Where only the PDA data is used as input to the optimization, lower normalized errors [calculated using the full Eq. (4)] are available for the low-shear-modulus case. Extension of the optimization process to include the distributed strain from the FBGs as input led to marginal reductions in error for the high-shear-modulus case compared to using the PDA input only. Similar to the PDA-only case, the overall normalized errors were lower when the G_1 profile was adopted, with inclusion of the FBG data being particularly beneficial for the blows analyzed later in the driving record (509 and 832).

It is worth considering independently the quality of the pile head match, which is traditionally used to assess pile capacity; Fig. 16 shows the match at the pile head obtained by both the manual and optimization process for the LD05 EOD blow. The manual case

Table 5. Comparison of mobilized resistances obtained by manual signal matching and optimization for EOD blow on LD05

	Mobilized resistances (kN)		
Case	Shaft	Base	Total
PDA input only—no optimization	342	254	596
PDA input only ($G = G_{max}$) 1a	253	254	507
PDA input only ($G = G_1$) 2b	285	254	539
PDA and FBG input ($G = G_{max}$) 2a	252	254	506
PDA and FBG input ($G = G_1$) 2b	277	254	531

gives the best coincidence in the time up to first reflection from the tip ($t_{m+2L/c}$, see Fig. 7). Optimization using the G_1 case (1b and 2b) typically gives a good match at the pile head, although it leads to a lower mobilized resistance and a poorer match close to the pile tip. The optimization process using $G = G_{\max}$ gives a generally poorer match to the upward force at the pile head and a lower mobilized resistance (Table 5). To more accurately determine mobilized resistance during the optimization process, it may be possible to refine the pile head match by adopting an alternative measure of the normalized error, which applies weighting to different portions of the record. The effect of varying the viscosity parameters α and β, was also explored during the optimization process. While both parameters were allowed to vary within fixed bounds but held constant with depth, this did not lead to a significant difference in the deduced (static) resistances mobilized.

Examples of the resulting shear resistance profiles for the optimized low-shear-modulus case are shown in Fig. 17. Fig. 18 shows examples of the measured and optimized ($G = G_1$) calculated force time histories for six gauge levels along the shaft for pile LD05 at EOD, which show significant improvements over Fig. 15. Some comment is appropriate with regard to the spike in mobilized shear stress at a depth of 6 m in Fig. 17(b). This was an unexpected outcome of the optimization process using the FBG data that did not occur when optimizing with the PDA data only. It is worth noting that limiting the shear stress in the optimization process to a maximum of 20 kPa over the relevant depths resulted in only a slight increase in the normalized error from 4.1% to 4.6% and a marginal decrease in the capacity of 0.3%. Given the reasonably uniform chalk profile, and the absence of any corresponding spike in the optimized results for blow (509) in Fig. 17(a), the spike appears to be a quirk of the FBG data, due to slight timing errors in the signals, the effects of residual strains that have been zeroed out, or the limited measurement resolution. The spike also appeared from optimization of the fit to the penultimate blow.

The previous analysis illustrates an effective optimization process and demonstrates the advantages of combining PDA and FBG measurements in cases where the shaft shear resistance distributions are highly nonuniform. The ALPACA piles' relatively large wall thickness led to lower axial strain resolution than would be typical in most industrial production pile cases, along with

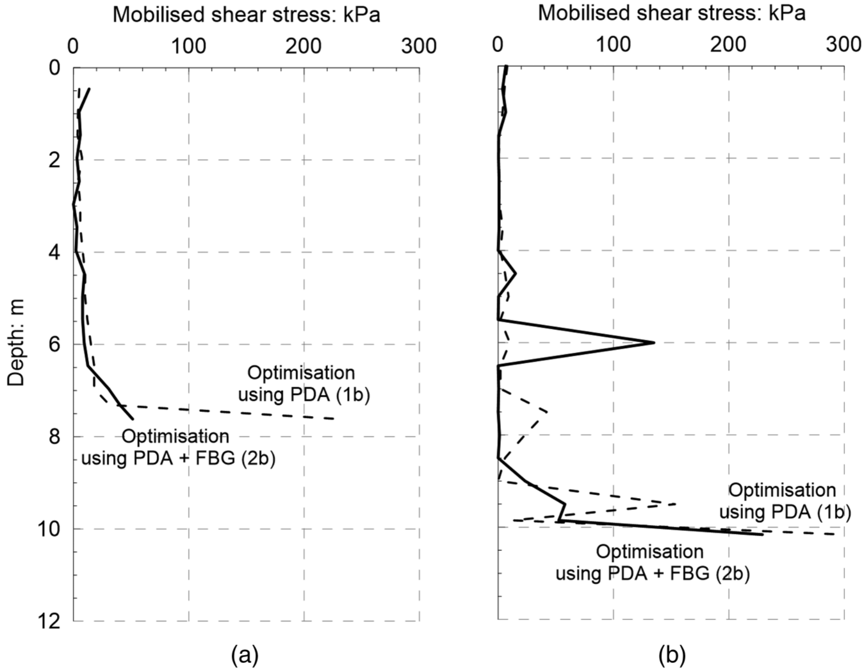

Fig. 17. Example profiles of mobilized shear resistance for IMPACT analyzes run with optimization: (a) blow 509; and (b) EOD blow.

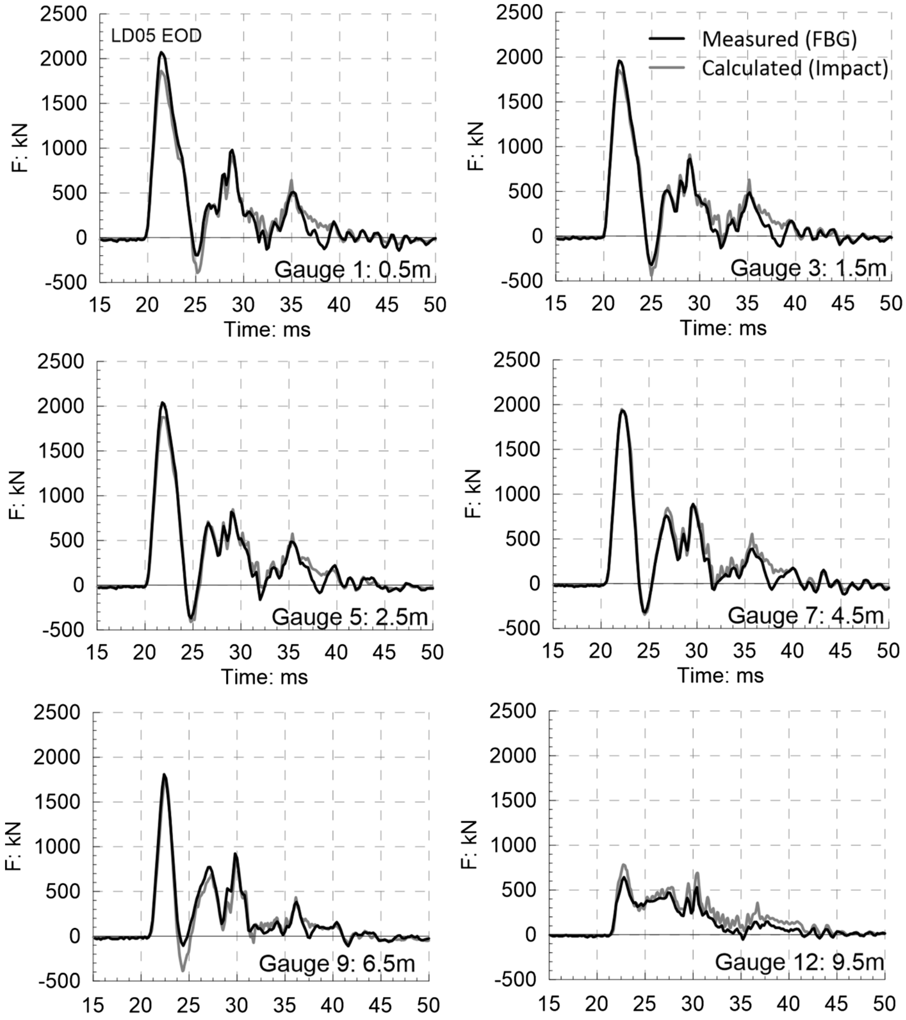

Fig. 18. Comparison of measured and optimized force time histories at various gauge levels at end of driving LD05.

relatively high apparent pile forces resulting from potential changes in pile temperature. Variations in the zero-strain values were removed by rezeroing the gauges after each blow during driving, but at the cost of eliminating any true residual locked-in forces and potentially affecting the deduced driving resistances listed in Table 5. However, any such effects would be reduced greatly when considering longer piles with lower wall thickness-to-diameter ratios. Here the FBG instruments would prove still more valuable, particularly when considering layered profiles. Of course, the availability of FBG data down the pile, for all hammer blows, would allow a completely automated and robust fitting of each hammer blow to be obtained. In this way, the complete evolution of the shaft resistance and base resistance during driving could be obtained. Naturally the sensors would prove equally valuable in any monitoring of static load testing or of in-service performance.

Conclusions

This paper describes the interpretation of fiber Bragg-grating measurements taken on 508-mm-diameter tubular steel piles ($L/D =$ 6–20) during impact driving at an established test site in Kent, UK. High-frequency measurements taken with the pile head PDA and pile shaft FBG sensors allowed detailed analysis of the signals recorded during the driving of each pile. The analysis presented was simplified by resetting the residual strains to zero after each hammer blow. The field experiments and analysis led to the following main conclusions:

1. All FBG sensors survived driving in the low-to-medium-density chalk. No damage was caused by the chalk's medium-sized, hard, and sharp flint inclusions.
2. Interrogating the FBG sensors at 5 kHz allowed the stress wave propagation to be resolved satisfactorily along the whole pile shaft lengths during each hammer blow.
3. The FBG measurements could be compared and correlated directly with high-frequency conventional PDA measurements.
4. Small changes in strain during driving due to extraneous effects such as temperature change could result in significant apparent pile force errors with the relatively thick-walled ALPACA piles, with residual tension and compression strains developing that increased with pile penetration.
5. Signal matching of individual blows through one-dimensional stress wave theory, employing the IMPACT software, allowed the shaft and base resistances to be inferred and further checked by means of the FBG instruments.
6. An optimization process was developed and applied to improve the signal matching for both the pile head PDA and shaft FBG sensors.
7. While neglecting residual straining may have influenced the results of the optimization process, the combined PDA and FBG approach offers significant advantages that may help to overcome the subjectivity implicit in conventional signal-matching analysis.
8. The new approach may be particularly valuable in cases in which driving resistances are nonuniform and pile wall thickness-to-diameter ratios are lower. The ability to resolve shaft distributions more reliably is likely to be especially helpful when considering layered ground profiles.

Data Availability Statement

Some or all data, models, or code generated or used during the study are proprietary or confidential in nature and may only be provided with restrictions.

Acknowledgments

The ALPACA project was funded by the Engineering and Physical Science Research Council (EPSRC) through Grant No. EP/P033091/1. The authors acknowledge the provision of additional financial and technical support by the following project partners: Atkins, Cathies, Fugro, GCG, Equinor, innogy, LEMS, Ørsted, Parkwind, Siemens, Scottish Power Renewables, and Vattenfall. The authors acknowledge gratefully the work of Socotec UK (formerly ESG) as the main contractor for the field testing program; Marmota Engineering AG as the subcontracted fiber optic strain gauge specialist; Green Piling, who installed the piles; and Lankelma UK and Fugro Geo-services, who carried out the cone penetration tests and boreholes, respectively. The authors are also grateful to Mr. Ken Vinck, who helped to supervise the site investigation.

Notation

The following symbols are used in this paper:

A = cross-sectional area of pile;
C_b = base dashpot;
c = wave speed in pile = $\sqrt{\frac{E}{\rho}}$;
c_h = coefficient of horizontal consolidation;
c_s = shaft dashpot;
D = pile diameter;
E = Young's modulus of pile;
F = force in pile;
F_{ave} = average PDA force on diametrically opposite sides of the pile;
F_d = force in pile due to upward-traveling wave;
F_{max} = maximum average measured force;
F_{up} = force in pile due to upward-traveling wave;
$F_{up,max}$ = maximum PDA force in pile due to upward-traveling wave;
F_1, F_2 = force measured on diametrically opposite sides of the pile;
f_s = sleeve friction;
G = shear modulus of chalk;
G_{max} = maximum (small strain) shear modulus of chalk;
G_s = particle density;
G_{vh} = shear modulus from shear wave velocity propagating vertically and polarized horizontally;
G_1 = secant shear modulus of chalk;
K_b = base spring constant;
k_s = shaft spring constant;
L = pile embedded length;
m_0 = subsidiary mass in the base resistance model;
n = number of strain gauge horizons;
p_0' = initial mean effective stress;
Q_b = base resistance;
$Q_{b,stat}$ = limiting base resistance in the base dynamic model;
q_{ba} = limiting bearing pressure mobilized over the piles' annular steel areas;
q_t = net cone resistance;
q_u = unconfined compressive strength;
R = external pile radius;
R_a = average center-line roughness;
R_i = internal pile radius;
R^* = equivalent radius of an open-ended pile = $\sqrt{(\boldsymbol{R})^2 - (\boldsymbol{R}_i)^2}$;

S_r = degree of saturation;
s_u = undrained shear strength;
t = time;
t_{wall} = wall thickness of the pile;
t_m = time at which maximum force F_m occurs;
t_0 = time for first increase in force;
t_{50} = time for 50% pore water pressure dissipation;
u_1 = pore water pressure in a CPT test measured at the cone tip;
u_2 = pore water pressure in a CPT test measured at the shoulder;
V = nondimensional velocity;
V_s = shear wave velocity;
v = velocity of pile or CPT (mm/s);
v_d = velocity in pile associated with downward-traveling wave;
v_{up} = velocity in pile associated with upward-traveling wave;
v_0 = dimensionless velocity (= 1 m/s);
w = displacement;
w_c = moisture content;
w_l = liquid limit;
w_p = plastic limit;
Z = pile impedance;
z = depth;
α = viscous parameter;
β = viscous parameter;
ε = strain;
ζ = overall normalized error;
ζ_f = average root mean square error between the measured and calculated F at each strain gauge;
$\zeta_{f,up}$ = average root mean square error between the measured and calculated F_{up} at the pile head;
ν = Poisson's ratio;
ρ = steel mass density;
ρ_s = total density;
τ = shaft shear friction;
τ_{inter} = shaft shear friction in the interface augmented by viscous effects;
τ_{stat} = limiting shaft shear friction in the dynamic model; and
φ' = angle of internal shearing resistance.

References

Alves, A. M., F. R. Lopes, M. F. Randolph, and B. R. Danziger. 2009. "Investigations on the dynamic behavior of a small-diameter pile driven in soft clay." *Can. Geotech. J.* 46 (12): 1418–1430. https://doi.org/10.1139/T09-069.

Baldwin, C. S., T. Salter, J. B. Niemczuk, P. C. Chen, and J. S. Kiddy. 2002. "Structural monitoring of composite marine piles using multiplexed fiber Bragg grating sensors: In-field applications." In *Smart Structures and Materials 2002: Smart Systems for Bridges, Structures, and Highways*, 82–91. Newport Beach, CA: International Society for Optics and Photonics.

Bowden, A. J., T. W. Spink, and R. N. Mortimore. 2002. "The engineering description of chalk: Its strength, hardness and density." *Q. J. Eng. Geol. Hydrogeol.* 35 (4): 355–361. https://doi.org/10.1144/1470-9236/00044.

Briaud J. L., and L. M. Tucker. 1984. "Residual stresses in piles and the wave equation." In *Proc. ASCE Symp. Deep Foundations*, 119–137. Reston, VA: ASCE.

Buckley R. M. 2018. "The axial behaviour of displacement piles in chalk." Ph.D. thesis, Dept of Civil and Environmental Engineering, Imperial College London.

Buckley, R. M., R. J. Jardine, S. Kontoe, P. Barbosa, and F. C. Schroeder. 2020. "Full-scale observations of dynamic and static axial responses of offshore piles driven in chalk and tills." *Géotechnique*. https://doi.org/10.1680/jgeot.19.TI.001.

Buckley, R. M., R. J. Jardine, S. Kontoe, and B. M. Lehane. 2018a. "Effective stress regime around a jacked steel pile during installation ageing and load testing in chalk." *Can. Geotech. J.* 55 (11): 1577–1591. https://doi.org/10.1139/cgj-2017-0145.

Buckley, R. M., R. J. Jardine, S. Kontoe, D. Parker, and F. C. Schroeder. 2018b. "Ageing and cyclic behaviour of axially loaded piles driven in chalk." *Géotechnique* 68 (2): 146–161. https://doi.org/10.1680/jgeot.17.P.012.

Buckley R. M., S. Kontoe, R. J. Jardine, M. Maron, F. C. Schroeder, and P. Barbosa. 2017. "Common pitfalls of pile driving resistance analysis–A case study of the Wikinger offshore windfarm." In *Proc. 8th Intl. Conf. Offshore Site Investigation and Geotechnics*, 1246–1253. London: Society of Underwater Technology.

Byrne, B. W., et al. 2019. "Monotonic lateral loaded pile testing in a stiff glacial clay till at Cowden." *Géotechnique*. https://doi.org/10.1680/jgeot.18.pisa.003.

Byrne, T., K. Gavin, L. Prendergast, P. Cachim, P. Doherty, and S. C. Pulukul. 2018. "Performance of CPT-based methods to assess monopile driveability in North Sea sands." *Ocean Eng.* 166 (2018): 76–91. https://doi.org/10.1016/j.oceaneng.2018.08.010.

Ciavaglia, F., J. Carey, and A. Diambra. 2017a. "Monotonic and cyclic lateral tests on driven piles in chalk." *Proc. ICE Geotech. Eng.* 170 (4): 353–366. https://doi.org/10.1680/jgeen.16.00113.

Ciavaglia, F., J. Carey, and A. Diambra. 2017b. "Time-dependent uplift capacity of driven piles in low to medium density chalk." *Géotech. Lett.* 7 (Mar): 1–7. https://doi.org/10.1680/jgele.16.00162.

Deeks, A. J., and M. F. Randolph. 1995. "A simple model for inelastic footing response to transient loading." *Int. J. Num. Meth. Geotech. Eng.* 19 (5): 307–329. https://doi.org/10.1002/nag.1610190502.

Doherty, P., et al. 2015. "Field validation of fibre Bragg grating sensors for measuring strain on driven steel piles." *Géotech. Lett.* 5 (2): 74–79. https://doi.org/10.1680/geolett.14.00120.

Dührkop J., S. Maretzki, and J. Rieser. 2017. "Re-evaluation of pile driveability in chalk." In *Proc. 8th Intl. Conf. Offshore Site Investigation and Geotechnics*, 666–673. London: Society for Underwater Technology.

Fellenius B. H. 1988. "Variation of CAPWAP results as a function of the operator." In *Proc. 3rd Int. Conf. on the Application of Stress Wave Theory to Piles*, 814–825. Ottawa: Bitech.

Fugro. 2012. *Laboratory testing report: Pile test site, chalk specific testing*. St. Nicholas at Wade, UK: Fugro Geoconsulting.

Jardine R. J., R. M. Buckley, B. Byrne, S. Kontoe, R. Macadam, and K. Vinck. 2019. "The ALPACA research project to improve driven pile design in chalk." In *Proc. 17th European Conf. on Soil Mechanics and Geotechnical Engineering*, 1–8. Reykjavik, Iceland: Icelandic Geotechnical Society.

Jardine, R. J., R. M. Buckley, S. Kontoe, P. Barbosa, and F. C. Schroeder. 2018. "Behaviour of piles driven in chalk." In *Engineering in Chalk*, 33–51. London: ICE Publishing.

Lee, W., W.-J. Lee, S.-B. Lee, and R. Salgado. 2004. "Measurement of pile load transfer using the fiber Bragg grating sensor system." *Can. Geotech. J.* 41 (6): 1222–1232. https://doi.org/10.1139/t04-059.

Liu, J., and M. Zhang. 2012. "Measurement of residual force locked in open-ended pipe pile using FBG-based sensors." *Electron. J. Geotech. Eng.* 17 (2012): 2145–2154.

Lord, J. A., C. R. L. Clayton, and R. N. Mortimore. 2002. *Engineering in chalk*. London: Construction Industry Research and Information Association.

Loukidis D., R. Salgado, and G. Abou-Jaoude. 2008. *Assessment of axially-loaded pile dynamic design methods and review of INDOT axially-loaded design procedure*. 62-1 10/08 JTRP-2008/6; FHWA/IN/JTRP-2008/6. West Lafayette, IN and Washington, DC: Purdue University in Cooperation with Indiana DOT and Federal Highway Administration.

Maiorano R., C. Viggiani, and M. Randolph. 1996. "Residual stress system arising from different methods of pile installation." In *Proc., 5th Int. Conf. on the Application of Stress-Wave Theory to Piles*, 518–528. Boca Raton, FL: CRC Press/A.A. Balkema.

Matthews M. C., and C. R. I. Clayton. 1993. “Influence of intact porosity on the engineering properties of a weak rock.” In *Proc., Int. Symp. Geotechnical Engineering of Hard Soils and Soft Rocks*, 693–702. Rotterdam, Netherlands: A.A. Balkema.

McAdam, R. A., et al. 2019. “Monotonic lateral loaded pile testing in a dense marine sand at Dunkirk.” *Géotechnique*. https://doi.org/10.1680/jgeot.18.pisa.004.

Middendorp P. 1987. *Numerical model for TNOWAVE*. Report BI-86-75. Delft, Netherlands: TNO-IBBC.

Mullins, G., C. L. Lewis, and M. D. Justason. 2002. “Advancements in statnamic data regression techniques.” In *Deep foundations 2002: An international perspective on theory, design, construction, and performance*, 915–930. Reston, VA: ASCE.

Randolph, M. F. 2008. *IMPACT—Dynamic analysis of pile driving, Manual*. Crawley, Australia: Dept. of Civil and Environmental Engineering, Univ. of Western Australia.

Randolph M. F., and H. A. Simons. 1986. “An improved soil model for one-dimensional pile driving analysis.” In *Proc. 3rd Intl. Conf. Numerical Methods in Offshore Piling*, 3–17. Nantes, France: Editions Technip.

Schilder C., H. Kohlhoff, D. Hofmann, F. Basedau, W. R. Habel, M. Baeßler, E. Niederleithinger, S. Georgi, and M. Herten. 2013. “Static and dynamic pile testing of reinforced concrete piles with structure integrated fibre optic strain sensors.” In *Proc., 5th European Workshop on Optical Fibre Sensors*, 1–4. Krakow, Poland: International Society for Optics and Photonics.

Schmidt-Hattenberger, C., T. Straub, M. Naumann, G. Borm, R. Lauerer, C. Beck, and W. Schwarz. 2003. “Strain measurements by fiber Bragg grating sensors for in situ pile loading tests.” In *Smart structures and materials 2003: Smart sensor technology and measurement systems*, 289–294. Bellingham, WA: International Society for Optics and Photonics.

SEtech. 2007. *Trial site investigation–Thanet offshore wind farm trial site*. Great Yarmouth, UK: SEtech (Geotechnical Engineers) Ltd.

Simons H. A., and M. F. Randolph. 1985. “A new approach to one dimensional pile driving analysis.” In *Proc., Int. Conf. on Numerical Methods in Geomechanics*, 1457–1464. Cambridge, UK: Univ. of Cambridge.

Teh, C. I., and G. T. Houlsby. 1991. “An analytical study of the cone penetration test in clay.” *Géotechnique* 41 (1): 17–34. https://doi.org/10.1680/geot.1991.41.1.17.

Tran, K. T., M. McVay, R. Herrera, and P. Lai. 2012. “Estimating static tip resistance of driven piles with bottom pile instrumentation.” *Can. Geotech. J.* 49 (4): 381–393. https://doi.org/10.1139/t2012-001.